Weighted Plancherel estimates and sharp spectral multipliers for the Grushin operators

The International Journal of Advanced Manufacturing Technology (2025) 138:1039–1054
https://doi.org/10.1007/s00170-025-15576-x

ORIGINAL ARTICLE

Assessment of simulation software for predicting induced distortions in laser-beam powder bed fusion of Ti6Al4V

Alberto Giubilini[1,2] · **Flaviana Calignano**[1,2] · **Manuela Galati**[1,2] · **Paolo Minetola**[1,2]

Received: 6 February 2025 / Accepted: 12 April 2025 / Published online: 26 April 2025

Abstract

The right first time (RFT) in the laser-beam powder bed fusion of metal powder (PBF-LB/M) process refers to achieving optimal part quality and minimal distortions in the first manufacturing attempt, which is critical for enhancing productivity and sustainability. This is particularly challenging due to the internal stresses and thermal gradients inherent to the process, which lead to significant distortions. This study addresses the challenge of predicting and mitigating these distortions for Ti6Al4V parts in the PBF-LB/M process. Calibration tests and experimental validations using Amphyon software were conducted, with the process involving software calibration, sensitivity analysis, and simulation validation through reverse engineering tools. Additionally, a pre-compensation method was applied to monitor and reduce distortion. The results demonstrated that Amphyon can predict distortions with a maximum deviation of up to 14% between simulated and experimental results, while pre-compensation reduces deformation by up to 70%. Finally, the simulation approach was validated through a real-world application, fabricating a cranial medical implant, showcasing its practical relevance. This work highlights the potential of simulation tools for optimizing PBF-LB/M processes, improving accuracy, and reducing material waste in industrial applications.

Keywords Laser-beam powder bed fusion of metal powder (PBF-LB/M) · Process simulation · Amphyon · 3D scanning · Ti6Al4V · Right first time

1 Introduction

The American Society of Testing Materials (ASTM) classifies all additive manufacturing (AM) processes into seven categories, based on the distinctive functional principles [1]. One of the leading AM technologies for metals in the industrial world is laser-beam powder bed fusion of metal powder (PBF-LB/M) [2]. With more than 20 years of process reliability, PBF-LB/M proved to be a versatile technique for different application fields, including automotive [3, 4], aerospace [5, 6], biomedical [7–9], and sport racing [10]. This process uses a high-power-density laser, whose source is usually an Ytterbium (Yb) fiber, to locally melt a metal powder and realize near-net shape components [11]. Similar to other AM processes, PBF-LB/M building process also requires preparatory and post-processing steps to obtain the final component [12]. The schematic representation in Fig. 1 outlines a general process with the sequence of its characteristic steps, starting with model creation and process optimization, followed by the preparation of machine, and loading of metal powder. Once the AM process is completed, post-processing ensues, including stress relieving [13], supports removal, de-powdering, and finishing of the component [14].

Some of the reasons for the great industrial success of PBF-LB/M include its final mechanical performance, which is equal or even higher than traditional manufacturing technologies, low surface roughness, high design freedom, and wide range of processable materials [15]. On the other hand, PBF-LB/M is a quite sensitive process and achieving the desired dimensional accuracy remains a challenge. This is influenced by various process parameters and material properties, which must be accurately controlled [16]. One of the most sensitive aspects of this

✉ Alberto Giubilini
alberto.giubilini@polito.it

[1] Department of Management and Production Engineering (DIGEP), Politecnico Di Torino, Corso Duca Degli Abruzzi 24, 10129 Turin, Italy

[2] Integrated Additive Manufacturing Centre (IAM@PoliTO), Politecnico Di Torino, Corso Duca Degli Abruzzi 24, 10129 Turin, Italy

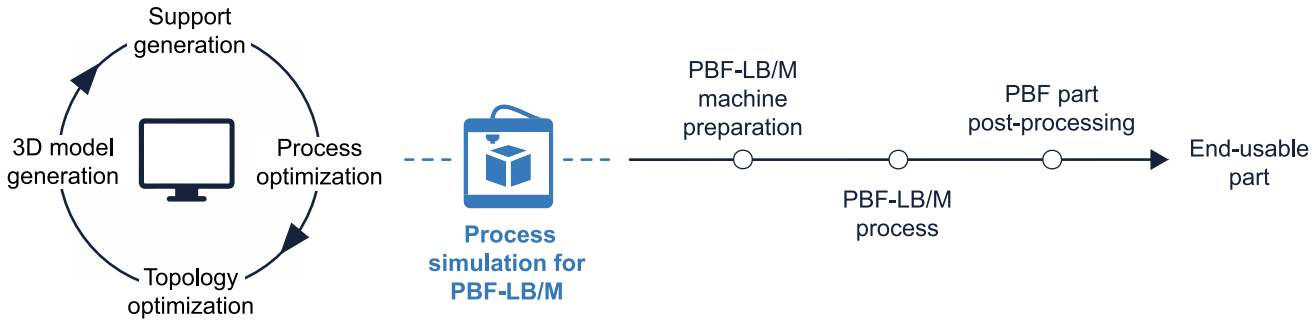

Fig. 1 Representation of the whole workflow for the production of a metal component using PBF-LB/M

technique is related to the thermal gradients that develop during the process, which can lead to deformation and residual stress [17]. Specifically, the concentrated laser action creates a heat-affected zone (HAZ) that expands and pushes down the material inducing a compressive state on the lower layers [18]. After cooling, HAZ shrinks and causes high tensile stresses in the neighboring area, thus inducing permanent deformation [19]. Figure 2 qualitatively describes the phenomenon described.

These induced deformations are important not only for the final properties of the component but also for the sustainability of the whole manufacturing process. Indeed, like other metal AM technologies, PBF-LB/M involves rather long production times and high material acquisition costs [20]. Consequently, any deviation from the desired geometry results in a significant waste of machine time, and resources [21]. In this regard, previous studies evidenced that the support structures and the connections with the building platform can help heat transfer, reducing thermal gradient and, consequently, local deformations [22–24]. However, large volumes of supports can increase the overall manufacturing cycle cost and build time [25]. Additional post-processing steps for support removal could generate more waste to be disposed of. Therefore, the capability to manufacture a part on the first attempt with the intended geometry is essential for increasing production reliability, reducing costs, and enhancing AM's competitiveness [26]. This principle is commonly referred to as "right first time" or RTF.

Better control over the final geometry and dimensional accuracy in AM cannot be reached using a single solution, but rather a combination of several strategies. These strategies may include lattice structure optimization [27, 28], part topological redesigning [29], and optimization of the process parameters such as laser power, scanning strategy and speed, hatching distance, and layer thickness [30]. Furthermore, recent advancements in computerized methodologies provided innovative solutions to this industrial challenge. For instance, Wang et al. developed a knowledge graph embedding learning system for defect diagnosis in AM [31], while Safdar et al. identified the requirements for implementing a machine learning operations platform to support process-based machine learning models in industrial metal AM [32]. Günaydın et al. optimized build orientation in PBF-LB/M using a non-dominated sorting genetic algorithm-II to minimize support volume and build time, thus influencing quality, waste, production time, and cost [33]. In a subsequent study, the authors explored 13 different optimization algorithms to determine the optimum build orientation, considering undercut area and build height as objective functions [34]. Jabón et al. proposed a novel integration approach of an Evolutive-Deformation framework with finite element methods (FEM) to address

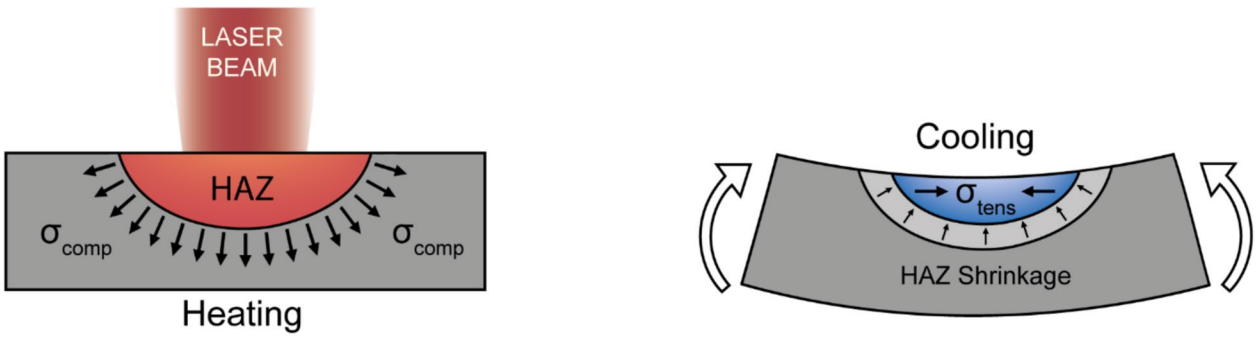

Fig. 2 Representation of the heat-affected zone (HAZ) during heating and cooling steps of PBF-LB/M

this issue effectively [35]. Numerical simulation software became indispensable for optimizing AM processes by providing insights into thermal history, melt pool dynamics, and solidification behavior. As a result, the number of commercial numerical codes that provide ready-to-use solutions is also increasing. For example, Amphyon is a commercial simulation software by Additive Works GmbH developed for predicting outcomes in the PBF-LB/M process. Its main aim is to support the process design within a virtual environment, thus reducing the need for trial-and-error iterations in selecting process parameters. By simulating different process parameters, such as materials absorption, heat transfer, molten fluid dynamic, and phase transformation, it is possible to predict some interesting final properties such as density, porosity, microstructure, residual stress, and deformation of printed parts [36]. However, the complexity of the PBF-LB/M process which cover several length and time scales is challenging to be represented in a complete manner and in a single environment. Therefore, numerical models are usually developed focusing on one or a few selected outcomes of the process, introducing procedures for enhancing the fit between the actual process and the simulated counterpart. Within this environment, it is possible to study the effect of several process conditions on the outcome, such as the presence and quantity of support structures or the final part distortion. Simulation results can also provide advice for improving the part quality. For instance, the software can compute the compensation for the distortion through part design modification. Each software possesses its own strengths and weaknesses depending on the specific application. In a prior study conducted by Peter et al., Amphyon 2018 and ANSYS Additive Print 19.1 demonstrated proficiency in predicting the recoater contact, whereas Autodesk Netfabb Simulation 2019 stood out for its user-friendly interface and quicker computation, particularly excelling in compensating for distortions in thin walls. However, it could be improved in the customization of laser exposure parameters. Sunata 2018 and Amphyon 2018 offered greater customization options for supports, yet they could benefit from enhanced control over support types [26]. Differences have also been observed within the same code environment using two different packages. In this regard, Mayer et al. observed how two ANSYS packages designed with the same aim can have quite different levels of accessibility from user-friendly or advanced expert in FEM [37]. Despite the growing interest in simulation-based optimization, research often presents simulation software as just one aspect of the broader workflow in metal AM part production [38, 39], without in-depth scrutiny. Consequently, the validation and evaluation of simulation software against experimental data remains crucial for widespread adoption in industrial settings.

This manuscript presents a comprehensive evaluation of Amphyon software for predicting the dimensional accuracy in PBF-LB/M of Ti6Al4V parts. The study aims to assess the software's accuracy in predicting the induced distortions and identify potential areas for improvement. Ti6Al4V was selected because it undergoes significant thermal stresses during the PBF-LB/M process, making it a suitable material for evaluating the accuracy and reliability of simulation software designed to predict process-induced distortions. To achieve this scope, an experimental campaign was used to calibrate the software for the application to Ti6Al4V. Also, the experimental data were used to evaluate the sensitivity of the numerical model. The validation of the results involved comparing the numerically predicted deformed shape with the actual part using reverse engineering (RE) tools, structured-light 3D scanning, and X-ray computer tomography scanning (X-CT scan). In addition, simulations were used to generate compensations aimed at correcting the resulting distortions. The modified STL output file, named pre-compensated geometry, served as input for manufacturing in PBF-LB system. This pre-compensated geometry embodies modifications to the original CAD model, enabling automatic recovery of component distortions during the process and facilitating the attainment of a final geometry more faithful to the original CAD model. Finally, the entire tested procedure was applied to a complex structure, a skull medical implant, to assess the feasibility of the investigated approach in real AM production.

2 Materials and methods

2.1 Materials and equipment

The material selected for the analysis was virgin Ti6Al4V powder by EOS (EOS GmbH, Krailling, Germany), processed on an EOSINT M270 Dual Mode machine (EOS GmbH, Krailling, Germany). This machine features a working chamber of $250 \times 250 \times 215$ mm^3, operating in a controlled Argon (Ar) atmosphere that limits the oxygen content to 0.1%, reducing the reactivity of the titanium powder. It is equipped with a 200 W Ytterbium (Yb) fiber laser with a focal spot size of 100 µm. To enhance mechanical properties and dimensional accuracy, the printing parameters can be adjusted based on the building zone. Three distinct zones are identified: contour, core, and skin. The contour defines the outermost boundary of the part, the core forms its innermost volume, whereas the skin constitutes the outer core of the part, significantly influencing surface finish [40]. The process parameter values of the core, skin, and contour for Ti6Al4V are presented in Table 1.

Table 1 EOSINT M270 Dual Mode process parameters for Ti6Al4V

	Laser power (W)	Laser spot size (μm)	Scan speed (mm/s)	Hatching distance (μm)
Core	170	100	1250	100
Skin	150	100	1000	100
Contour	120	100	1250	Not applicable

2.2 Simulation software

The Amphyon software (Oqton GmbH, Bremen, Germany) was used to carry out the PBF-LB/M manufacturing process simulation. It comprises five different modules designed to guide the user throughout the AM workflow. The first module analyzes the CAD model and evaluates the part orientation, while the second module generates and optimizes support structures. These are followed by two modules that predict mechanical and thermal properties, respectively, considering process and simulation parameters as well as stress-relieving treatments to estimate final deformation. The last module serves as a "pre-deformation" tool, compensating for deformation deviations from the nominal geometry. It generates a pre-compensated model, adapting support structures accordingly. The final output is a modified STL file that, after manufacturing, achieves the intended shape while accounting for deformation.

2.3 Process simulation

Amphyon only allows the use of a single set of process parameters for the entire simulation, without distinguishing between core, skin, or contour regions. Given this constraint, the core parameters listed in Table 1 were selected as representative of the overall process, as the core constitutes the predominant volume fraction of the component. This choice ensures that the simulation reproduces the real process as accurately as possible. While this approach does not capture localized parameter variations, it provides a reasonable approximation of the process within the limitations of the software. Table 2 shows the process parameters and Ti6Al4V properties, as declared by the producer's datasheet, used in Amphyon for conducting the simulation. All simulations and data analyses were run on a workstation equipped with an Intel®Core i7 - 8700 K and 3.70 GHz, 32 GB RAM, NVIDIA Quadro P620, an HDD storage and Windows 10 64-bit as operating system.

The mesh resolution is a critical parameter in balancing simulation accuracy and computational efficiency. In Amphyon software, this parameter can be varied from 0 (coarse) to 10 (fine). For all simulations, an adaptive mesh with a constant value of 0.6 was chosen. This choice ensured each simulation could be completed within approximately 90 min on a standard desktop computer, representing an optimal trade-off between accuracy and computational time.

Table 2 Amphyon process and material parameters

Process parameters	Value
Laser power (W)	170
Scan speed (mm/s)	1250
Hatching distance (μm)	100
Layer thickness (μm)	30
Build plate temperature (°C)	100
Material parameters	Value
Young modulus (GPa)	110
Yield stress (GPa)	1.06
Poisson coefficient	0.3

2.4 Calibration analysis

Calibration is a required procedure in Amphyon to fine-tune the software's response based on the selected material and processing conditions. This process involves fabricating three different cantilever specimens and assessing their respective bending behavior according to the applied hatching strategy. The reference specimen ($180 \times 7.2 \times 8$ mm^3) was obtained from Amphyon's official documentation. It features a "T-shaped" geometry with horizontal top surfaces, built parallel to the build plate and supported by thin vertical walls. Figure 3 shows the three distinct hatching strategies, i.e., "Parallel," "Orthogonal," and "Average":

- Parallel hatching (Fig. 3a) involves laser scanning along the longitudinal axis of the cantilever.
- Orthogonal hatching (Fig. 3b) employs a scanning strategy perpendicular to this direction.
- Average hatching can be achieved in two ways: by rotating the hatching direction 90° between layers or by alternating the scan direction within each layer in small adjacent regions (Fig. 3c).

The different hatching strategies are expected to generate diverse thermal distribution, leading to different residual stress levels and deformations. To assess the as-built condition, no stress relief treatments were applied. After fabrication, the cantilever specimens were removed from the build platform using an ECUT 32D CNC Wire Cut EDM machine (Genesi Ltd., Monza e Brianza, Italy) following the longitudinal direction, as recommended by Amphyon's documentation. Then, the specimen bending was measured using a structured light 3D scanner, ATOS Compact Scan 2 M (Zeiss AG, Oberkochen, Germany). The scan data was then processed with GOM Inspect

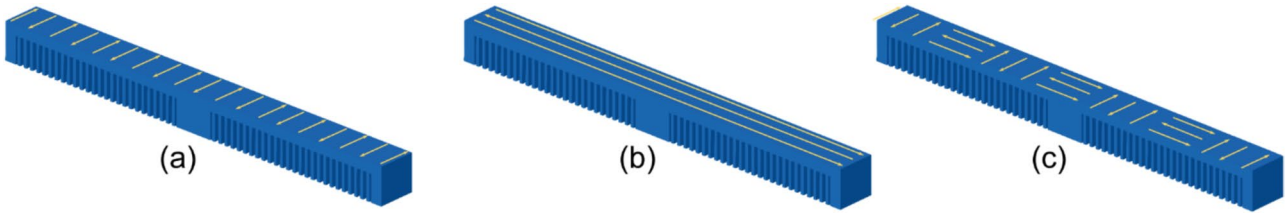

Fig. 3 Hatching strategies of calibration PBF-LB/M specimen: parallel hatching (**a**), orthogonal hatching (**b**), and average hatching (**c**)

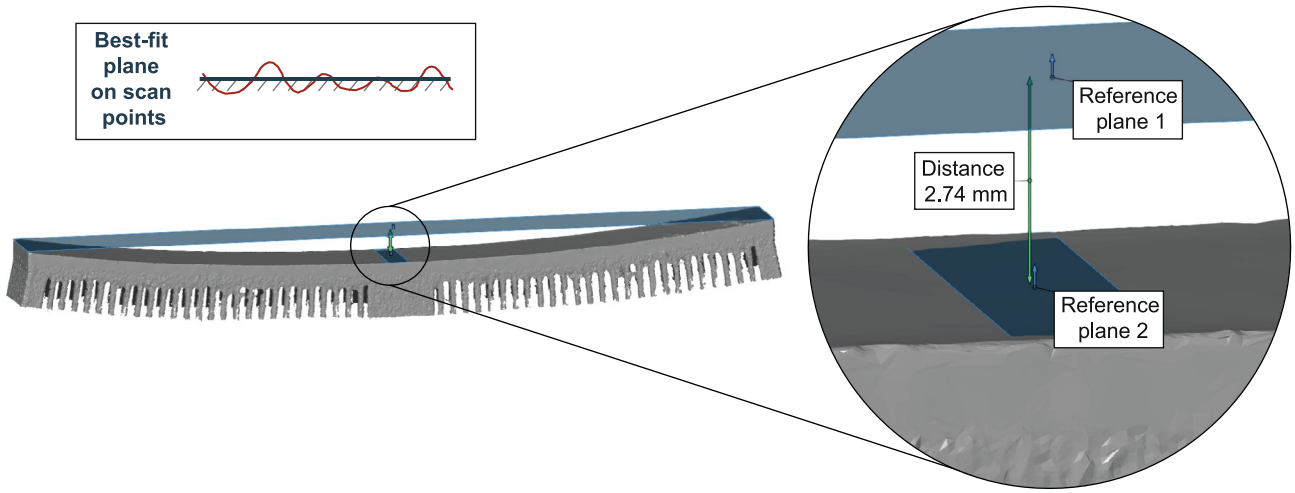

Fig. 4 Measuring of maximum deflection for cantilevers

software (Zeiss AG, Oberkochen, Germany) to determine the maximum deflection, as required by the calibration procedure. Figure 4 illustrates the methodology employed to calculate the maximum deflection. This was determined as the maximum distance between two planes belonging to the same cantilever. A first reference plane was defined by best fitting two sets of points located at the extremities of the cantilever, where distortion was most pronounced. Then, a second plane was generated by selecting points in the middle of the top surface, where distortion was minimal. Due to the high number of acquired data points and mesh irregularities, the least-squares method was employed to ensure optimal plane fitting with minimal error. Finally, the deflection values for each hatching strategy were entered into the Amphyon software simulation settings to complete the calibration process.

2.5 Analysis of numerical sensitivity

To evaluate the sensitivity of the simulation results, variations were applied to the process parameters while keeping all other parameters at their nominal values. The simulation parameters, namely laser power, scan speed, hatching distance, and layer thickness, were modified by ± 10% and ± 20% from the nominal values specified in Table 2, resulting in a total of 16 simulations. The parameter values used for the sensitivity analysis are detailed in Table 3. The sensitivity of the numerical results was evaluated by observing key outcomes, including build time (t_b), maximum residual stress (σ_r), and the maximum temperature within the part (T) at the end of each simulation layer. It is important to note that in Amphyon's thermal module, only a macro-scale temperature state can be simulated. Therefore, the temperatures displayed in the simulation represent the temperature of the upper layer before the next layer is processed.

Table 3 Set of process parameters used for simulation sensitivity study

Parameter	− 20%	− 10%	Nominal value	+ 10%	+ 20%
Laser power (W)	136	153	170	187	204
Scan speed (mm/s)	1000	1125	1250	1375	1500
Hatching distance (µm)	80	90	100	110	120
Layer thickness (µm)	24	27	30	33	36

It is important to highlight that in real-world applications, selecting certain combinations of process parameters may not be feasible due to the need for consistency in process outcomes and the proper melting of the metal powder. In this study, the selected parameters are used solely to assess the software's response to variations in input. For example, an increase in speed is expected to result in lower temperatures and, consequently, reduced stress compared to nominal conditions. The numerical sensitivity analysis was performed with a reference geometry named "Longitudinal Square Box" (LS-Box), which is available as an STL file in Amphyon's online documentation. The LS-Box is a hollow prism with a square cross-section, and its faces are oriented at 45° to the build direction, eliminating the need for support structures during the PBF-LB/M process. A 6.35-mm vertical edge was used to connect the part to the building platform, and the wall thickness is uniformly set at 1.67 mm. Figure 5 shows the geometry and its overall dimensions.

2.6 Experimental validation through dimensional and accuracy characterization

The experimental validation activities employed the same reference geometry (LS-Box) used in the numerical sensitivity analysis. This geometry was fabricated using Ti6Al4V powder on the EOSINT M270 Dual Mode machine, with the EOS scanning strategy featuring a 67° rotation between layers. After manufacturing, the actual geometry of the resulting parts was acquired and digitized through X-CT and light 3D scanning. The digitized model was then compared against the nominal reference geometry to assess accuracy and deformations. The X-CT machine used was the Phoenix v|tome|x S240 (GE Baker Hughes-Waygate Technologies, Wunstorf, Germany), which captures images with a resolution of 1000 × 1000 pixels. The scanning parameters included a voxel size of 67 µm, 235 kV voltage, and 110 mA current. The X-ray images were reconstructed into a 3D model using datos|reconstruction software (GE Baker Hughes-Waygate Technologies, Wunstorf, Germany). For visualization and analysis, the software VG Studio Max software (version 3.4) by Volume Graphics (Hexagon Metrology-Volume Graphics, Heidelberg, Germany) was used. Optical 3D scanning was carried out with the ATOS Compact Scan 2 M, a structured light scanner that uses stereoscopic vision and blue LED light. Data analysis, distortion evaluation, and inspection were performed using GOM Inspect software.

3 Results and discussions

3.1 Calibration results

The calibration step began with the production of the cantilever geometry using three different laser scanning strategies, as outlined in Table 1. These strategies involve varying scan vector lengths, which result in different maximum bending values for the specimens. Figure 6 shows the actual geometry of the three specimens after they were separated from the build platform, displaying the distortions induced by the PBF-LB/M process.

The hatching strategy aligned parallel to the longitudinal direction of the cantilever exhibited the highest deflection. This outcome can be attributed to the longer scan vector length, which leads to higher residual stresses and thermal gradients compared to the orthogonal strategy, which possesses a shorter scan vector length (Fig. 3). These results are consistent with the previous literature [18, 41–44]. The average strategy, which combines both scan directions, results in a deflection that is approximately intermediate between the other two. Table 4 presents the maximum deflections for each cantilever, along with the corresponding hatching strategy.

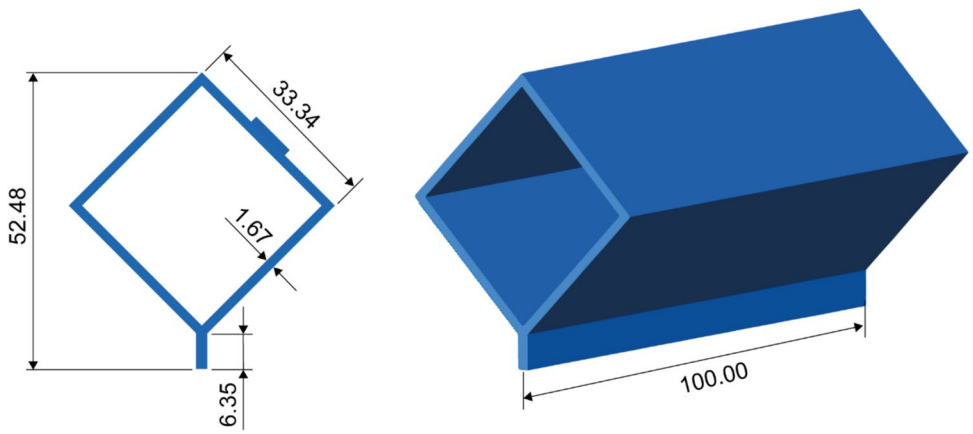

Fig. 5 Reference geometry for simulation sensitivity analysis and validation experimental activities (dimensions are in millimetres)

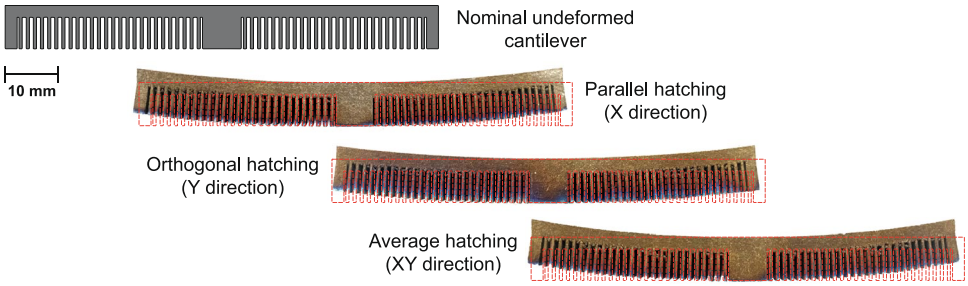

Fig. 6 Ti6Al4V calibration specimens manufactured with three different scanning strategies via PBF-LB/M

Table 4 Cantilever maximum deflections for Amphyon calibration

Cantilever hatching strategies	Deflection (mm)
Parallel	2.74
Orthogonal	2.09
Average	2.28

3.2 Numerical sensitivity analysis

A sensitivity analysis was carried out to evaluate the computational capability and accuracy of Amphyon software in predicting the impact of parameter changes in the PBF-LB/M process. The key findings from this analysis are summarized in the bar graphs of Fig. 7, with dotted lines representing reference values obtained using the nominal process parameters listed in Table 2. It is important to highlight that these findings are specific to simulations and may not translate directly translate to practical applications for all parameter combinations. In fact, some parameter sets may not even ensure proper material fusion, a limitation that the software does not necessarily highlight. Therefore, the purpose of this analysis is to assess the theoretical sensitivity of the software in generating different simulation outputs through systematic parameter variations, rather than to suggest feasible real-world process implementations.

The analysis focused on the maximum temperature (T) estimated at the end of each simulation layer, which serves as an indicator of the macroscopic temperature state in the component. It was observed that an increase in laser power resulted in a corresponding rise in T, with a maximum increase of over 10 °C from the reference value (Fig. 7a). This trend nicely mirrors the findings reported by Bian et al., who reported that increasing laser power results in higher temperatures and a larger molten pool size, regardless of the scanning strategy used [45]. Although specific temperature values vary due to differences in material and simulation software, the observed trends are consistent with those in the literature [45]. Conversely, reducing scan speed or hatching distance by 20% increased the energy per unit volume on the powder bed, resulting in an increase in T to 180 °C, compared to 165 °C in the reference case. Although direct comparisons with previous studies are challenging due to variations in material, simulation software, or parameter sets, these findings are comparable to those of Khorsani et al., who observed an increase in melt pool peak temperature with decreasing scan speed [46]. The effect of layer thickness on T was minimal, and no significant correlation was found between layer thickness and temperature. It is fundamental to recognize that the simulation involved simplifications, such as neglecting heat dissipation through the machine structure and the varying heat transfer conditions for different regions (core or contour). Therefore, while the simulation provided stable results, these simplifications may limit its representativity of the actual process.

Additional trends emerged in the assessment of build time (t_b), which reflects the actual job duration. Figure 7b presents the main results. As expected, t_b is influenced by the ratio of part height to layer thickness, with a reduction in layer thickness leading to an increase in the number of layers and a corresponding extension of build time. Varying layer thickness from −20 to +20% resulted in a reduction of t_b from over 8 to 5.5 h. Hence, layer thickness was found to be the most influential parameter on build time. Similarly, hatching distance and scan speed also influenced the printing time, consistent with previous studies [47–49]. However, the sensitivity analysis was virtual and did not account for whether the material was melted. Assuming the material was always melted, higher scan speed and increased hatching distance reduced t_b slightly, from 7 to 6.5 h. Laser power did not significantly influence printing time.

Regarding the maximum residual stress (σ_r), no direct correlation was established between σ_r and the macro-scale temperature represented by T (Fig. 7c). The σ_r values remained within a narrow range, fluctuating approximately ± 16% around a central value of 53.6 kPa, as represented by the red band in Fig. 7c. This range indicates that σ_r had a minimal influence on the final deformation in all simulations. For example, Zhang et al. reported that temperature variations significantly influenced σ_r [50]. However, such variations were not observed in this study, making a direct comparison difficult. The consistent maximum deformation of 2.85 mm further supports the conclusion that minor variations in T do not substantially affect σ_r.

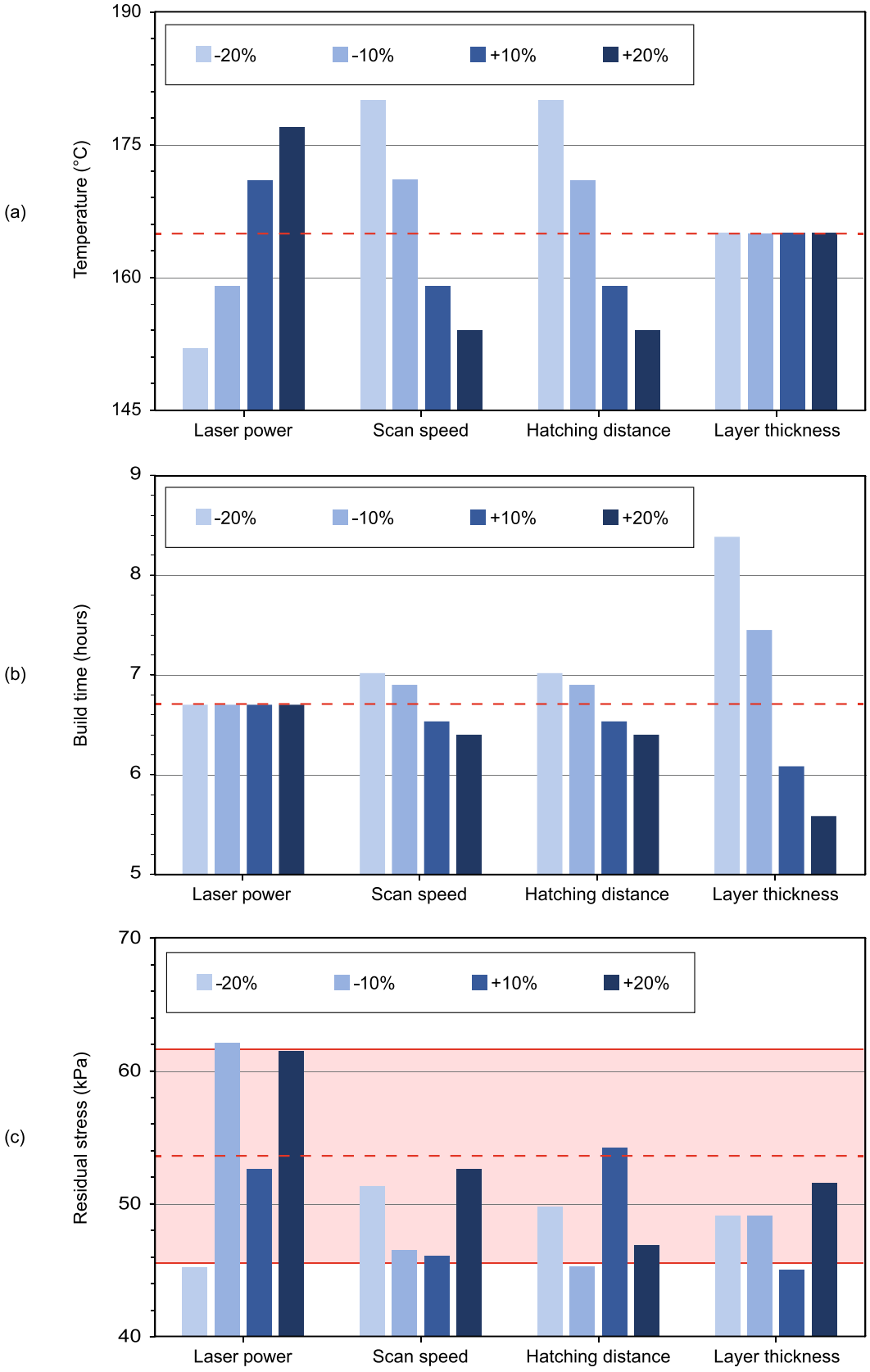

Fig. 7 Sensitivity analysis results: maximum temperature within the component evaluated at the end of each simulation layer (**a**); build time (**b**); maximum residual stress (**c**). The dotted lines are representative of the reference values obtained with nominal process parameters

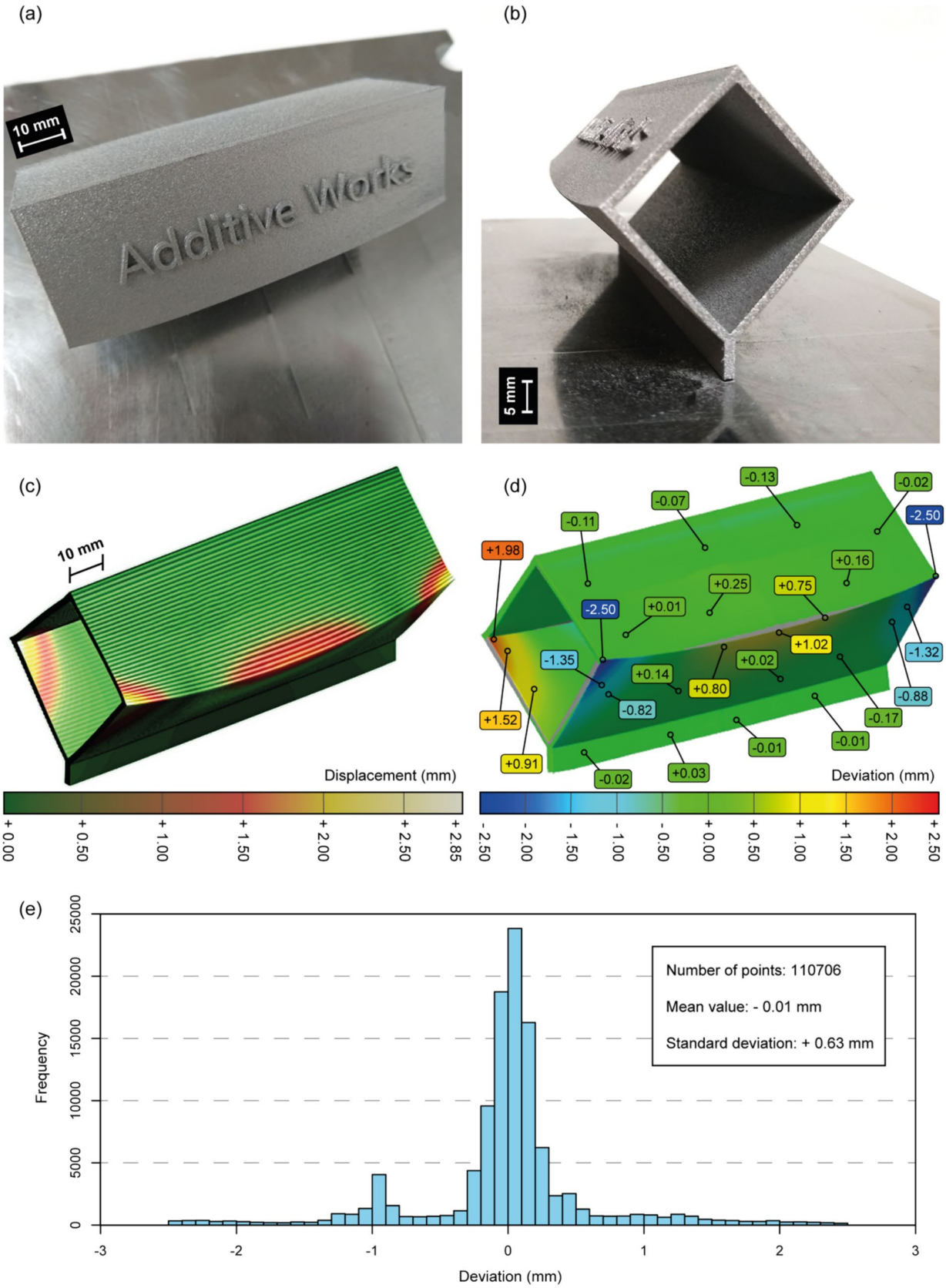

Fig. 8 Photographs of the square tube replica in Ti6Al4V by EOSINT M270 (**a**, **b**). Computed displacement by Amphyon simulation with nominal parameters (**c**). Deviations for actual part geometry compared with nominal CAD model (**d**). Deviation distribution histogram of the experimental validation LS-Box (**e**)

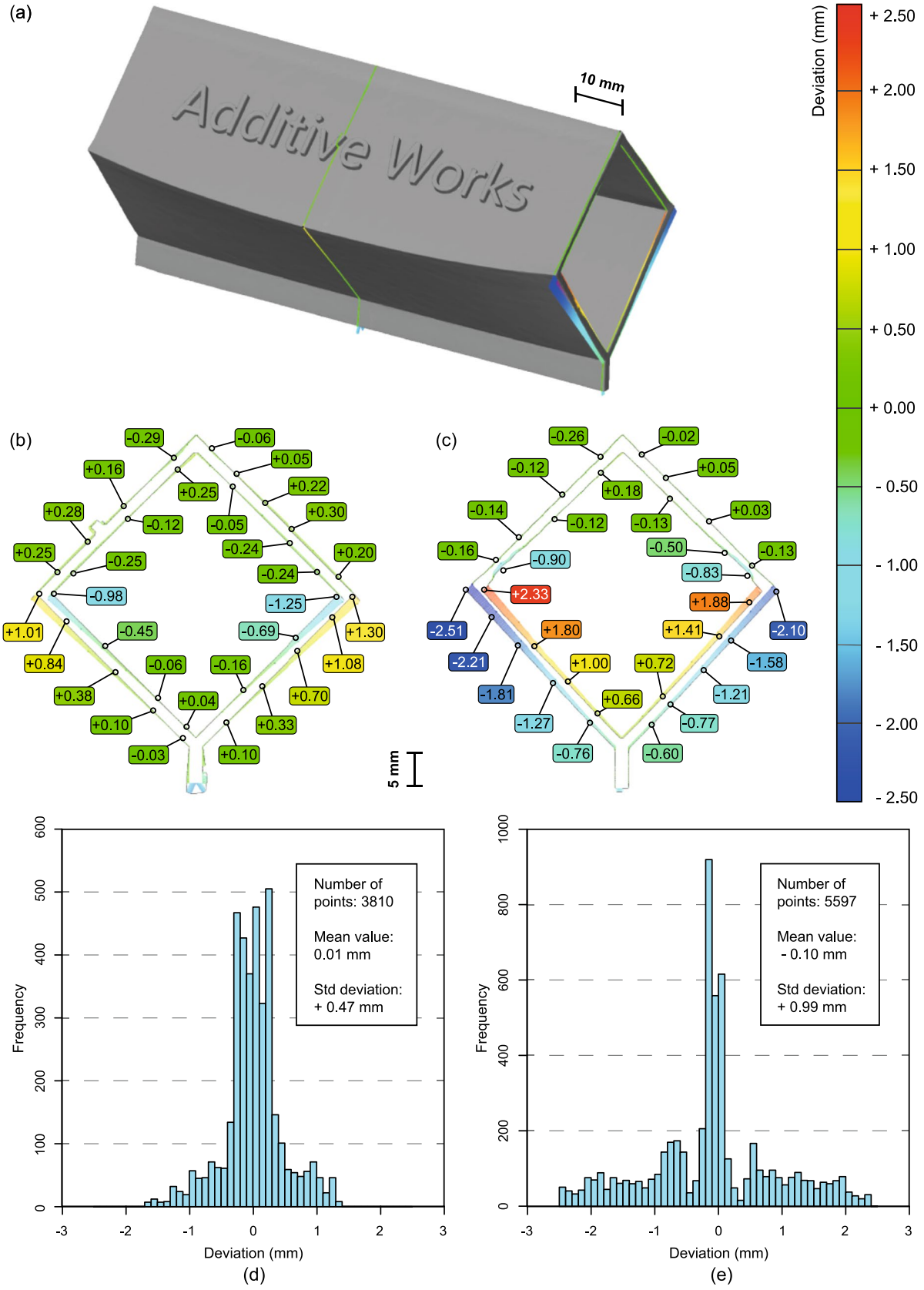

Fig. 9 CT scan data of the fabricated LS-Box (**a**) and two different inspection sections: middle (**b**), and initial (**c**). Deviation distribution histogram of the experimental validation LS-Box at two different inspection sections: middle (**d**), and initial (**e**)

3.3 Experimental validation

The LS-Box geometry was manufactured to assess the distortion induced by the PBF-LB/M stress on thin-wall components. The manufactured part is shown in Fig. 8a and Fig. 8b. On the actual part, the longitudinal straight edge on the sides of the square cube (Fig. 5) bent outwards and deformed in a curved line (Fig. 8b). This deformation was correctly predicted in simulation results (Fig. 8c). The fabricated part was then 3D scanned, and the scan data was used to compute the actual deformations to the nominal ideal geometry. The STL file of the scan data was imported into GOM Inspect software for alignment and comparison with the original CAD model. The results of this comparison are shown in the deviation map of Fig. 8d.

The comparison between the nominal CAD and the actual dimensions of the 3D printed component (Fig. 8d) revealed a maximum deformation of about 2.50 mm. However, the mean deviation was −0.01 mm, with a standard deviation of 0.63 mm, as shown in the deviation distribution histogram in Fig. 8e. Conversely, the Amphyon simulation (Fig. 8c) forecasted a maximum deformation value of approximately 2.85 mm, primarily concentrated at the ends of the longitudinal edges on the unsupported sides of the square shape. Although there is a maximum deviation of 14% between the simulated and experimental results, the deformation areas

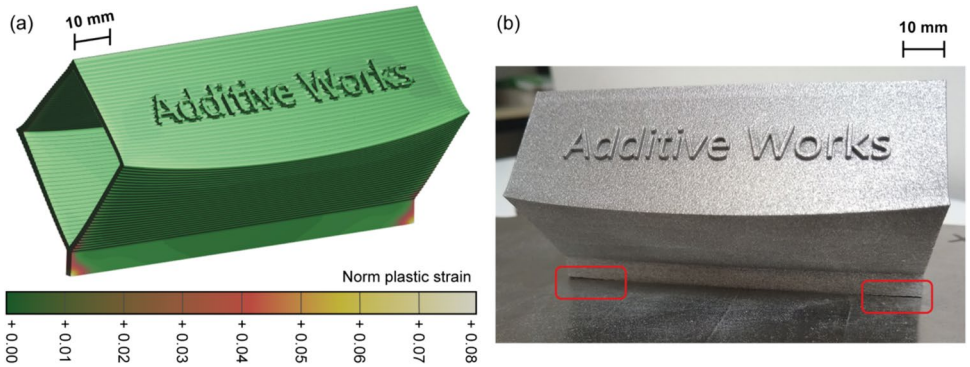

Fig. 10 Prediction of part detachment from the build platform: map of the normalized plastic strain from Amphyon software (**a**) and photo of the critical areas on the actual part (**b**)

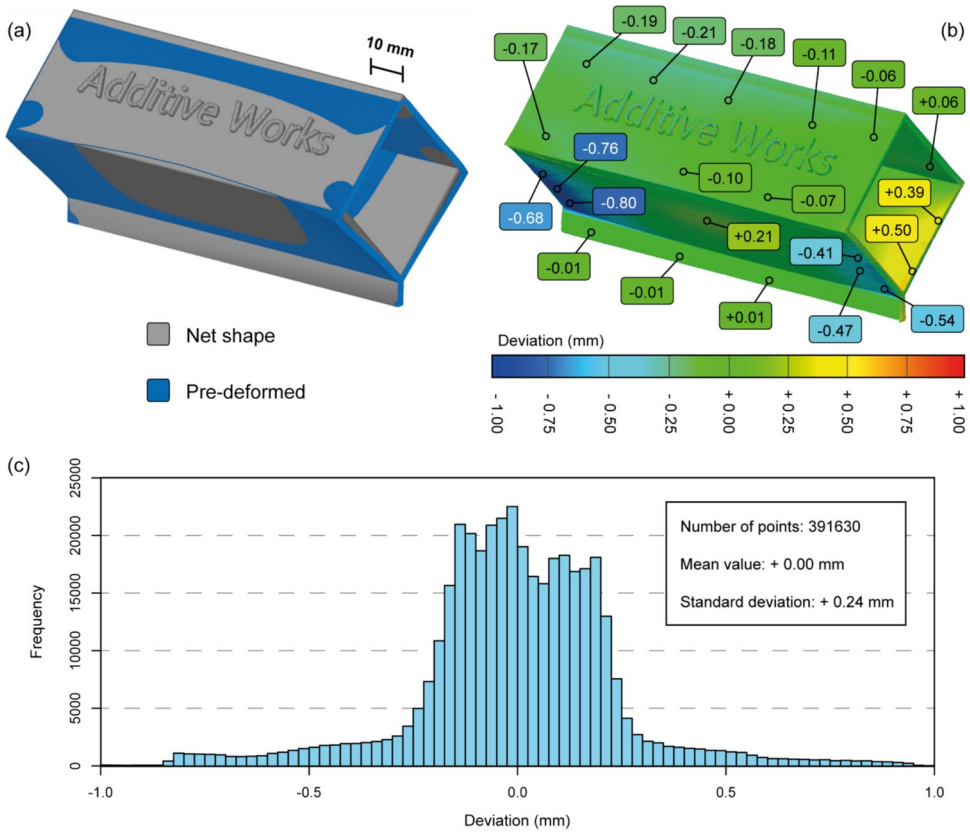

Fig. 11 Comparison between net-shape and pre-deformed models (**a**). Deviation map of the pre-deformed manufactured component to the nominal net-shape (**b**). Deviation distribution histogram of the pre-deformed manufactured LS-Box (**c**)

identified in the GOM Inspect colored map (Fig. 8d) align well with those predicted by Amphyon (Fig. 8c). It is important to note that the laser used in the PBF-LB/M machine has an inherent spot size of 0.1 mm, which can influence the formation of sharp edges and contribute to deviations. The observed discrepancies between the simulation and experimental results primarily stem from the model's inability to account for certain physical phenomena occurring at different scales. In particular, the simulation does not capture critical microscale processes such as melt pool dynamics and powder particle behavior, which significantly influence thermal distribution, material consolidation, and final part properties. These unmodeled phenomena introduce variability that contribute to the observed deviations. Despite these limitations, simulation reliability is typically assessed by comparing its predictions with experimental results within an acceptable margin of error. According to previous studies, deviations in the range of 10–15% [51] are considered reasonable for such simulations. In this context, the results of the experimental validation indicate that, with the cantilever calibration procedure, the Amphyon simulation software can effectively predict distortions in the most stressed zones of PBF-LB/M-built components with good dimensional accuracy. For a more detailed analysis, Fig. 9 presents two different sections of the replica, highlighting the deformations from the net shape. In both sections, a similar deviation from the original model was observed, with higher deformations located in the initial section (Fig. 9c) when compared to the middle one (Fig. 9b). This difference is further highlighted in the histograms shown in Fig. 9d and e, where the initial section has a mean deviation of -0.1 ± 0.99 mm. In contrast, the middle section shows a mean value that is an order of magnitude lower, with the standard deviation reduced by half.

A significant outcome arose from the simulation of plastic deformation, as indicated by the *Norm Plastic Strain* parameter of Amphyon software. In the red areas of Fig. 10a, the simulation results reported a final plastic strain of approximately 8%. This value has the realistic potential to induce detachment or delamination of the material layer because the EOS datasheet for Ti6Al4V reports an elongation at break of 9%. Consistent with these simulation results, the actual part detached from the build platform in the zones indicated by the red squares in Fig. 10b. Once again, the software's simulation capability was validated by accurately predicting the displacement of the most critical areas.

The Amphyon software has the functionality for generating a *pre-distorted and compensated* geometry. When produced on a PBF-LB/M machine, the compensated geometry is intended to yield the nominal shape. Hence, it was deemed valuable to extend the experimental validation and monitoring of part distortion by considering the fabrication of the compensated shape. To this aim, the pre-deformed shape (Fig. 11a) was produced through PBF-LB/M on the EOS M270 machine with the same parameters in Table 1. The fabricated geometry was then 3D scanned and compared to the nominal CAD model. The comparison results are shown in the deviation map of Fig. 11b.

The new analysis revealed that a reduction of over 70% in the actual deformation can be achieved, as well as a substantial reduction in the standard deviation shown by the histogram in Fig. 11c, when compared to the one in Fig. 8c, which was not pre-deformed. Specifically, a maximum deviation of about 0.80 mm was observed in the actual part produced from the compensated geometry. It is important to note that in the deviation from nominal dimensions, approximately ± 50 µm, is attributable to the surface roughness of a component fabricated by PBF-LB/M [52]. However, the impacted areas differ from the previous ones as down-facing sides exhibited higher deviations compared to the up-facing ones. The worst accuracy of unsupported down-facing surfaces in comparison to up-facing surfaces is typical of the PBF-LB/M process [53]. Table 5 provides a summary of the average deformation values and their standard deviations for the comparison of the original uncompensated geometry in Fig. 8d and the compensated shape in Fig. 11b.

The compensation of the large deformation of the longitudinal edge of the LS-box geometry in Fig. 11a helps to reduce part deviation, especially in the case of down-facing surfaces. Both the average value of the deformation and its standard deviation are lower for the compensated geometry demonstrating the effectiveness of Amphyon software in computing the pre-deformed shape for the LS-box.

3.4 Real case application

After the assessment of the validity of simulation results for the simple reference geometry of the LS-box, a real case was considered in the PBF-LB/M production of a cranial implant in Ti6Al4V. The titanium plate has overall dimensions of 132

Table 5 Deviation results for down-facing and up-facing surfaces of the original uncompensated geometry and compensated one

Part deformation	Uncompensated LS-Box geometry		Compensated LS-Box geometry	
	Down-facing surfaces	Up-facing surfaces	Down-facing surfaces	Up-facing surfaces
Average value (mm)	+ 0.15	+ 0.02	− 0.00	+ 0.02
Standard deviation (mm)	+ 0.78	+ 0.20	+ 0.31	+ 0.14

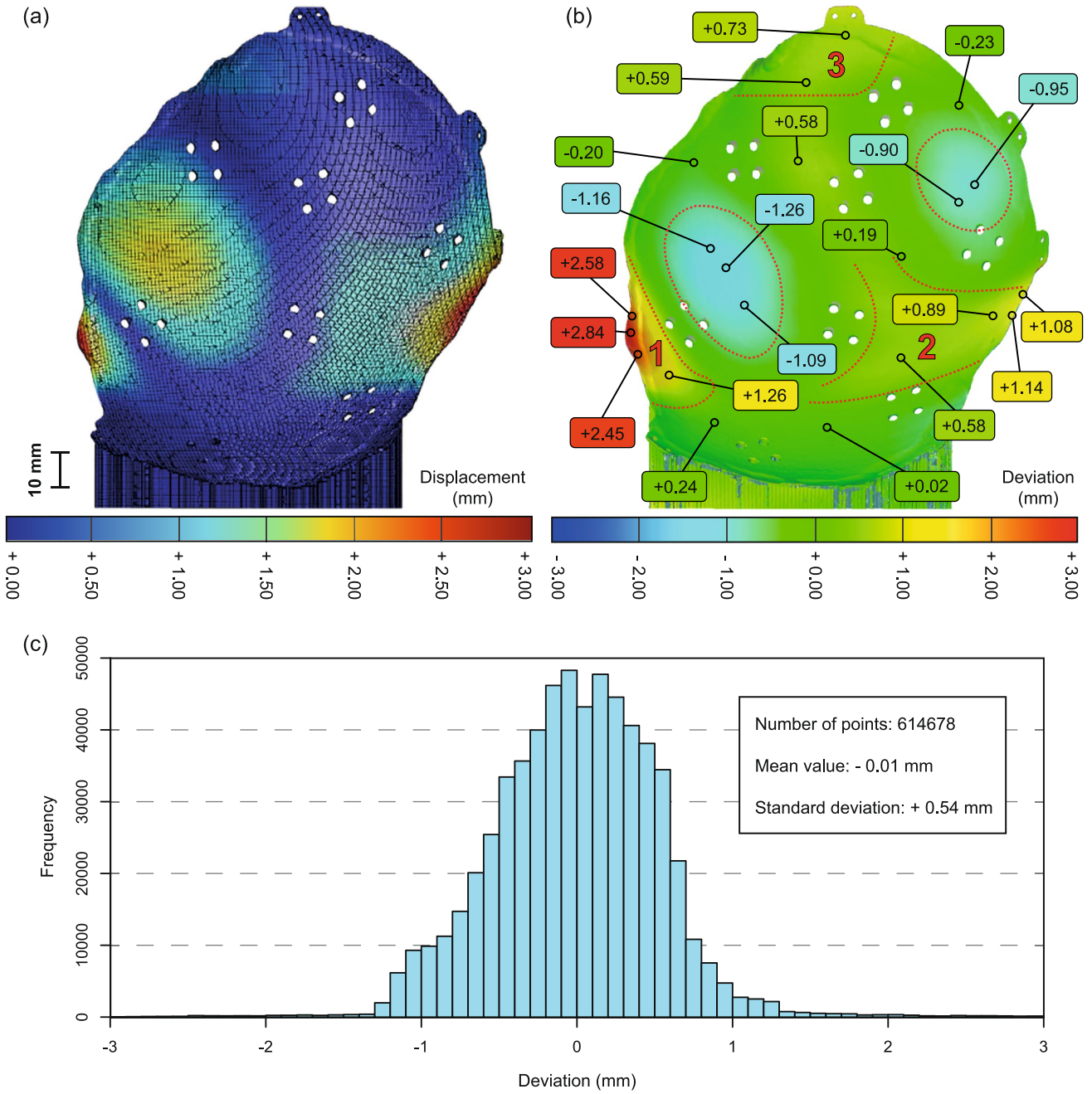

Fig. 12 Cranial implant comparison and validation. Simulation on Amphyon software of the final deformation (**a**). Colored map of the comparison between the scan data of the actual part scan and the nominal CAD model (**b**). Deviation distribution histogram of the cranial implant (**c**)

$\times 144 \times 72$ mm^3 and an average thickness of about 1.15 mm. The cranial implant was produced with the same machine and parameters used for the other parts of this study (Table 1).

The deformations resulting from the PBF-LB/M production of the cranial implant were computed by Amphyon simulation and are shown in Fig. 12a. The actual part was then 3D scanned with the ATOS Compact scanner and the scan data was aligned for comparison with the nominal ideal geometry of the plate. The comparison results in Fig. 12b show an average deviation of -0.01 mm and a standard deviation of 0.56 mm, also graphically represented in the histogram of Fig. 12c.

The experimental validation through the actual deviation results in Fig. 12b showed a good correspondence with the forecast of Amphyon simulation (Fig. 12a). The manufactured

implant exhibited deformations in the same main three areas predicted by the simulation. The borders of these three areas are traced by a red dotted line in Fig. 12b. Moreover, the displacement values of the simulation results and those of the produced implant were almost comparable. In area "1," the maximum deformation reached 3.00 mm, slightly higher than the displacement measured by simulation, which was 2.84 mm. Generally, the simulated deformations align well with the real case with an average gap of 0.40 mm. In conclusion, it can be asserted that this real case study confirmed what had already been pointed out in the validation step. While exhibiting some inaccuracies in predicting the absolute deformation values, the simulation can correctly forecast the deformation zones and the relative magnitudes of deviations. These results are valuable for a better understanding of the influence of PBF-LB/M process on the final part shape, contributing to the prevention of unexpected errors for reaching the ideal "right first-time" goal.

4 Conclusions

This study assessed the capability of Amphyon simulation software to predict distortions in PBF-LB/M of Ti6Al4V using the EOSINT M270 machine. A structured workflow was followed, including calibration, sensitivity analysis, and validation, to evaluate the accuracy and reliability of Amphyon software. The focus was on understanding deformation behavior in thin-walled geometries, which are particularly prone to distortions in the PBF-LB/M process. The software's predictive performance was assessed through systematic testing. To summarize the main findings of this study, the following key results were observed:

- While layer height variation did not affect the maximum temperature estimated at the end of each simulation layer (T), it significantly affected build time (t_b). Conversely, scan speed and hatching distance inversely impacted both t_b and T.
- Validation of actual components versus simulated ones showed a maximum deviation of 14%, with pre-compensation reducing deformations by up to 70%.
- Application to a cranial implant case revealed slightly higher deviations from experimental validation tests, averaging 0.40 mm with a maximum of 1.00 mm.
- Software limitations include the inability to define region-specific process parameters, process oversimplification, and lack of control over specific scanning strategies. Despite these constraints, the simulation effectively identified critical deformation zones and provided a valuable tool for compensating distortions in complex geometries.

Overall, this study developed a customized methodology for distortion analysis in PBF-LB/M, offering quantitative insights into deformation behaviors and process optimization for Ti6Al4V. While this material is widely used in PBF-LB/M and serves as a representative example, further exploration with other metals is necessary to enable broader generalization. Despite Amphyon's limitations, this paper emphasized the advantage of the simulation approach, offering potential efficiency and sustainability benefits for the PBF-LB/M process by minimizing material waste, user effort, and printing failure. This approach holds particular value for biomedical and aerospace applications, where precision and cost-efficiency are critical.

Acknowledgements The authors gratefully acknowledge Eng. Vito Stiuso for his valuable contributions to the setup of simulations and the inspection of actual part deviations.

Funding Open access funding provided by Politecnico di Torino within the CRUI-CARE Agreement.

Declarations

Competing interests The authors declare no competing interests.

References

1. ISO (2021) BS EN ISO/ASTM 52900:2021: Additive manufacturing - general principles - fundamentals and vocabulary. International Organization for Standardization, Geneva. https://www.iso.org/obp/ui/#iso:std:iso-astm:52900:dis:ed-2:v1:en
2. Abd-Elaziem W, Elkatatny S, Abd-Elaziem A-E et al (2022) On the current research progress of metallic materials fabricated by laser powder bed fusion process: a review. J Mater Research Technol 20:681–707. https://doi.org/10.1016/j.jmrt.2022.07.085
3. Bassoli E, Defanti S, Tognoli E et al (2021) Design for additive manufacturing and for machining in the automotive field. Appl Sci 11. https://doi.org/10.3390/app11167559
4. Adelmann B, Hellmann R (2022) Function integration in additive manufacturing: design and realization of an LPBF built compressed air motor. Materials 15. https://doi.org/10.3390/ma15196632
5. Pradeep PI, Kumar VA, Sriranganath A et al (2020) Characterization and qualification of LPBF additively manufactured AISI-316L stainless steel brackets for aerospace application. Trans Indian Natl Acad Eng 5:603–616. https://doi.org/10.1007/s41403-020-00159-x

6. Wang D, Wei X, Liu J et al (2022) Lightweight design of an AlSi10Mg aviation control stick additively manufactured by laser powder bed fusion. Rapid Prototyp J 28:1869–1881. https://doi.org/10.1108/RPJ-02-2022-0064
7. Safaei K, Abedi H, Nematollahi M et al (2021) Additive manufacturing of NiTi shape memory alloy for biomedical applications: review of the LPBF process ecosystem. JOM 73:3771–3786. https://doi.org/10.1007/s11837-021-04937-y
8. Liu C, Ling C, Chen C et al (2022) Laser additive manufacturing of magnesium alloys and its biomedical applications. Mater Sci Addit Manuf 1. https://doi.org/10.18063/msam.v1i4.24
9. Calignano F, Galati M, Iuliano L, Minetola P (2019) Design of additively manufactured structures for biomedical applications: a review of the additive manufacturing processes applied to the biomedical sector. J Healthc Eng 2019:9748212. https://doi.org/10.1155/2019/9748212
10. Markovits T, Szederkényi B (2022) Investigation of generative design for powder bed fusion technology in case of Formula student race car components using Ti6Al4V alloy. J Manuf Process 80:220–231. https://doi.org/10.1016/j.jmapro.2022.05.058
11. Calignano F, Manfredi D, Ambrosio EP et al (2017) Overview on additive manufacturing technologies. Proc IEEE 105:593–612. https://doi.org/10.1109/JPROC.2016.2625098
12. Mercurio V, Calignano F, Iuliano L (2023) Sustainable production of AlSi10Mg parts by laser powder bed fusion process. Int J Adv Manuf Technol 125:3117–3133. https://doi.org/10.1007/s00170-023-11004-0
13. Laleh M, Sadeghi E, Revilla RI et al (2023) Heat treatment for metal additive manufacturing. Prog Mater Sci 133:101051. https://doi.org/10.1016/j.pmatsci.2022.101051
14. Kumbhar NN, Mulay A V (2018) Post processing methods used to improve surface finish of products which are manufactured by additive manufacturing technologies: a review. J Inst Eng (India): Ser C 99:481–487. https://doi.org/10.1007/s40032-016-0340-z
15. Schneck M, Gollnau M, Lutter-Günther M et al (2019) Evaluating the use of additive manufacturing in industry applications. Procedia CIRP 81:19–23. https://doi.org/10.1016/j.procir.2019.03.004
16. Momeni K (2021) Sensitivity of laser powder bed fusion additive manufactured HAYNES230 to composition and print parameters. J Mater Res Technol 15:6453–6463. https://doi.org/10.1016/j.jmrt.2021.11.080
17. Ettaieb K, Lavernhe S, Tournier C (2021) A flash-based thermal simulation of scanning paths in LPBF additive manufacturing. Rapid Prototyp J 27:720–734. https://doi.org/10.1108/RPJ-04-2020-0086
18. Zaeh MF, Branner G (2010) Investigations on residual stresses and deformations in selective laser melting. Prod Eng Res Devel 4:35–45. https://doi.org/10.1007/s11740-009-0192-y
19. Roy M, Wodo O (2020) Data-driven modeling of thermal history in additive manufacturing. Addit Manuf 32:101017. https://doi.org/10.1016/j.addma.2019.101017
20. Calignano F, Mercurio V (2023) An overview of the impact of additive manufacturing on supply chain, reshoring, and sustainability. Clean Logist Supply Chain 7:100103. https://doi.org/10.1016/j.clscn.2023.100103
21. Dejene ND, Lemu HG (2023) Current status and challenges of powder bed fusion-based metal additive manufacturing: literature review. Metals (Basel) 13. https://doi.org/10.3390/met13020424
22. Dimopoulos A, Salimi M, Gan T-H, Chatzakos P (2023) Support structures optimisation for high-quality metal additive manufacturing with laser powder bed fusion: a numerical simulation study. Materials 16. https://doi.org/10.3390/ma16227164
23. Khobzi A, Farhang Mehr F, Cockcroft S et al (2022) The role of block-type support structure design on the thermal field and deformation in components fabricated by laser powder bed fusion. Addit Manuf 51:102644. https://doi.org/10.1016/j.addma.2022.102644
24. Bartsch K, Lange F, Gralow M, Emmelmann C (2019) Novel approach to optimized support structures in laser beam melting by combining process simulation with topology optimization. J Laser Appl 31. https://doi.org/10.2351/1.5096096
25. Atzeni E, Iuliano L, Marchiandi G et al (2014) Additive manufacturing as a cost-effective way to produce metal parts. In: High value manufacturing: advanced research in virtual and rapid prototyping - Proceedings of the 6th international conference on advanced research and rapid prototyping, VR@P 2013. pp 3–8. https://doi.org/10.1201/b15961-4
26. Peter N, Pitts Z, Thompson S, Saharan A (2020) Benchmarking build simulation software for laser powder bed fusion of metals. Addit Manuf 36. https://doi.org/10.1016/j.addma.2020.101531
27. Taşçı M, Erdaş MU, Kopar M et al (2024) Optimum design of additively manufactured aerospace components with different lattice structures. 66:876–882. https://doi.org/10.1515/mt-2023-0364
28. Aslan B, Yıldız AR (2020) Optimum design of automobile components using lattice structures for additive manufacturing. 62:633–639. https://doi.org/10.3139/120.111527
29. Mangla SK, Kazancoglu Y, Sezer MD et al (2023) Optimizing fused deposition modelling parameters based on the design for additive manufacturing to enhance product sustainability. Comput Ind 145:103833. https://doi.org/10.1016/j.compind.2022.103833
30. du Plessis A, Razavi N, Benedetti M et al (2022) Properties and applications of additively manufactured metallic cellular materials: a review. Prog Mater Sci 125:100918. https://doi.org/10.1016/j.pmatsci.2021.100918
31. Wang R, Cheung CF (2023) Knowledge graph embedding learning system for defect diagnosis in additive manufacturing. Comput Ind 149:103912. https://doi.org/10.1016/j.compind.2023.103912
32. Safdar M, Paul PP, Lamouche G et al (2024) Fundamental requirements of a machine learning operations platform for industrial metal additive manufacturing. Comput Ind 154:104037. https://doi.org/10.1016/j.compind.2023.104037
33. Günaydın AC, Yıldız AR, Kaya N (2022) Multi-objective optimization of build orientation considering support structure volume and build time in laser powder bed fusion. 64:323–338. https://doi.org/10.1515/mt-2021-2075
34. Günaydın AC, Yıldız AR (2024) A comparison of recent optimization algorithms for build orientation problems in additive manufacturing. 66:1539–1556. https://doi.org/10.1515/mt-2024-0099
35. Jabón J, Corbera S, Barea R, Martín-Rabadán J (2023) An evolutive-deformation approach to enhance self-supporting areas in additive manufacturing designs. Comput Ind Eng 182:109386. https://doi.org/10.1016/j.cie.2023.109386
36. Ninpetch P, Kowitwarangkul P, Mahathanabodee S et al (2020) A review of computer simulations of metal 3D printing. AIP Conf Proc 2279:050002. https://doi.org/10.1063/5.0022974
37. Mayer T, Brändle G, Schönenberger A, Eberlein R (2020) Simulation and validation of residual deformations in additive manufacturing of metal parts. Heliyon 6:. https://doi.org/10.1016/j.heliyon.2020.e03987
38. Nicoletto G, Riva E, Uriati F (2022) Lightweight design and additive manufacturing of a fatigue-critical automotive component. SAE Int J Adv & Curr Prac in Mobility 5(3):1048–1054. https://doi.org/10.4271/2022-37-0026
39. Uriati F, Zambrelli L, Nicoletto G, Garibaldi M (2021) Design, production, and fatigue testing of an optimized structural component made of L-PBF AlSi10Mg. In: Procedia Structural Integrity 34:184–190. https://doi.org/10.1016/j.prostr.2021.12.027

40. Bremen S, Eibl F, Gayer Ch, Heußen D, Lantzsch T, Masseling L, Munk J, Vogelpoth A, Pichler T, Pirch N, Risse J, Schmithüsen T, Schniedenharn M, Such A, Tenbrock Ch, Tenbrock U, Weiß Ch, Wissenbach K (2024) Laser Powder Bed Fusion (LPBF). In: Poprawe R, Häfner C, Wester, R (eds) Tailored Light 2. RWTHedition. Springer, Cham. pp 305–396. https://doi.org/10.1007/978-3-030-98323-9_7
41. Wang L, Jiang X, Zhu Y et al (2018) Investigation of performance and residual stress generation of AlSi10Mg processed by selective laser melting. Adv Mater Sci Eng 2018:7814039. https://doi.org/10.1155/2018/7814039
42. Jia H, Sun H, Wang H et al (2021) Scanning strategy in selective laser melting (SLM): a review. Int J Adv Manuf Technol 113:2413–2435. https://doi.org/10.1007/s00170-021-06810-3
43. Guo M, Ye Y, Jiang X, Wang L (2019) Microstructure, mechanical properties and residual stress of selective laser melted AlSi10Mg. J Mater Eng Perform 28:6753–6760. https://doi.org/10.1007/s11665-019-04423-2
44. Stephenson PL, Haghdadi N, DeMott R et al (2020) Effect of scanning strategy on variant selection in additively manufactured Ti-6Al-4V. Addit Manuf 36:101581. https://doi.org/10.1016/j.addma.2020.101581
45. Bian P, Shi J, Liu Y, Xie Y (2020) Influence of laser power and scanning strategy on residual stress distribution in additively manufactured 316L steel. Opt Laser Technol 132:106477. https://doi.org/10.1016/j.optlastec.2020.106477
46. Khorasani M, Ghasemi A, Leary M et al (2021) Numerical and analytical investigation on meltpool temperature of laser-based powder bed fusion of IN718. Int J Heat Mass Transf 177:121477. https://doi.org/10.1016/j.ijheatmasstransfer.2021.121477
47. Taghian M, Mosallanejad MH, Lannunziata E et al (2023) Laser powder bed fusion of metallic components: latest progress in productivity, quality, and cost perspectives. J Mater Res Technol 27:6484–6500. https://doi.org/10.1016/j.jmrt.2023.11.049
48. Pragana JPM, Pombinha P, Duarte VR et al (2020) Influence of processing parameters on the density of 316L stainless steel parts manufactured through laser powder bed fusion. Proc Inst Mech Eng B J Eng Manuf 234:1246–1257. https://doi.org/10.1177/0954405420911768
49. Leicht A, Fischer M, Klement U et al (2021) Increasing the productivity of laser powder bed fusion for stainless steel 316L through increased layer thickness. J Mater Eng Perform 30:575–584. https://doi.org/10.1007/s11665-020-05334-3
50. Zhang W, Tong M, Harrison NM (2020) Scanning strategies effect on temperature, residual stress and deformation by multi-laser beam powder bed fusion manufacturing. Addit Manuf 36:101507. https://doi.org/10.1016/j.addma.2020.101507
51. Dinesh S, Sahu J (2025) Thermomechanical simulation and experimental validation of distortion and residual stress for LPBF additive manufactured Inconel 718. Mater Today Commun 42:111512. https://doi.org/10.1016/j.mtcomm.2025.111512
52. Nandhakumar R, Venkatesan K (2023) A process parameters review on selective laser melting-based additive manufacturing of single and multi-material: microstructure, physical properties, tribological, and surface roughness. Mater Today Commun 35:105538. https://doi.org/10.1016/j.mtcomm.2023.105538
53. Calignano F, Iuliano L, Galati M et al (2020) Accuracy of downfacing surfaces in complex internal channels produced by laser powder bed fusion (L-PBF). Procedia CIRP 88:423–426. https://doi.org/10.1016/j.procir.2020.05.073